Physics in Medicine &
Biology

Modeling the stress and forces on multi-channel TMS coil arrays in high-field MRI scanners

IOP Publishing Phys. Med. Biol. 69 (2024) 175001 https://doi.org/10.1088/1361-6560/ad6b72

Physics in Medicine & Biology

IPEM Institute of Physics and Engineering in Medicine

OPEN ACCESS

RECEIVED
10 April 2024

REVISED
2 July 2024

ACCEPTED FOR PUBLICATION
5 August 2024

PUBLISHED
14 August 2024

PAPER

Modeling the stress and forces on multi-channel TMS coil arrays in high-field MRI scanners

Maria A Koponen[1,*], Juuso T Korhonen[1], José A Vilchez Membrilla[3], Heikki Sinisalo[1], Jaakko Paasonen[2], Clemente Cobos Sánchez[3], Olli Gröhn[2], Risto J Ilmoniemi[1] and Victor H Souza[1]

[1] Department of Neuroscience and Biomedical Engineering, Aalto University School of Science, Espoo, Finland
[2] A. I. Virtanen Institute for Molecular Sciences, University of Eastern Finland, Kuopio, Finland
[3] Engineering School, University of Cadiz, Cádiz, Spain
[*] Author to whom any correspondence should be addressed.

E-mail: maria.a.koponen@aalto.fi

Keywords: transcranial magnetic stimulation, TMS, multi-locus TMS, multi-channel TMS, functional magnetic resonance imaging, TMS-fMRI, finite element modeling

Supplementary material for this article is available online

Abstract

Transcranial magnetic stimulation (TMS) is a non-invasive method for stimulating the cortex. Concurrent functional magnetic resonance imaging can show changes in TMS-induced activity in the whole brain, with the potential to inform brain function research and to guide the development of TMS therapy. However, the interaction of the strong current pulses in the TMS coil in the static main magnetic field of the MRI produces high Lorentz forces, which may damage the coil enclosure and compromise the patient's safety. We studied the time-dependent mechanical behavior and durability of two multi-locus TMS (mTMS) coil arrays inside a high-field MRI bore with finite element modeling. In addition, coil arrays were built and tested based on the simulation results. We found that the current pulses produce shock waves and time-dependent stress distribution in the coil plates. The intensity and location of the maximum stress depend on the current waveform, the coil combination, and the transducer orientation relative to the MRI magnetic field. We found that 30% glass-fiber-filled polyamide is the most durable material out of the six options studied. In addition, novel insights for more durable TMS coil designs were obtained. Our study contributes to a comprehensive understanding of the underlying mechanisms responsible for the structural failure of mTMS coil arrays during stimulation within high static magnetic fields. This knowledge is essential for developing mechanically stable and safe mTMS-MRI transducers.

1. Introduction

Transcranial magnetic stimulation (TMS) is a non-invasive neuromodulation method with versatile neuroscience and clinical applications (Chail *et al* 2018, Iglesias 2020). In TMS, strong current pulses applied through coil windings produce changing magnetic fields through the cerebral tissue, inducing an electric field that stimulates cortical neurons (Ilmoniemi *et al* 1999). Combining TMS with neuroimaging provides a unique assessment of the spatial and temporal neuromodulatory effects on neuronal activity. Specifically, with functional magnetic resonance imaging (fMRI), whole brain activity can be indirectly assessed through neurovascular coupling with a spatial resolution of about 1 mm (Seewoo *et al* 2018, Afuwape *et al* 2021). Thus, TMS–fMRI provides important measures of brain function in healthy and neurological conditions (Mizutani-Tiebel *et al* 2022).

Designing TMS coils to operate safely in the scanner requires careful consideration due to the high mechanical stresses on the coil enclosure plates, which arise from the movement of the wires. During the TMS pulse, with a typical rise time of less than 100 μs, an electric current of up to several kiloamperes flows through the coil windings (Koponen *et al* 2015). For instance, inside a 3 T MRI scanner, the interaction

between the static magnetic field and the TMS current pulse creates strong Lorentz forces and stress on the figure-of-eight coil windings up to 130% and 420%, respectively, compared to outside the scanner (Crowther *et al* 2013). Such high stress might break the coil casing and expose the subject or patient to mechanical or electrical safety risks (Bergmann *et al* 2021, Mizutani-Tiebel *et al* 2022). Only a few studies have analyzed the mechanical behavior of TMS coils under such conditions, showing the Lorentz force and von Mises stress on individual coils at different orientations relative to the external MRI field when a continuous sinusoidal (Crowther *et al* 2012, Cobos Sánchez *et al* 2020, Afuwape *et al* 2021) and direct current (Crowther *et al* 2013) is applied. We recently observed that approximating a TMS pulse by direct or sinusoidal currents does not capture the transient and dynamic mechanical effects resulting from the fast-changing TMS fields (Koponen 2023). To foster the development of safe and mechanically durable coils, a realistic assessment of the interplay between the TMS pulse and the MRI static field is needed.

A second critical technical challenge in TMS–MRI applications is that positioning the TMS coil inside the MRI bore is inconvenient due to the restricted space, and usually, removing the subject from the scanner to change the coil orientation or location is required. Precise control of the TMS coil position is crucial to ensure that stimulation is delivered to the intended cortical target and that cortical mappings can be effectively performed to study brain function (Moisa *et al* 2009). A mechanical holder can assist in coil positioning (Lee *et al* 2023). However, the holder can only be adjusted outside the bore and involves a laborious and relatively slow manual process, making it impossible to stimulate distinct brain areas with millisecond intervals, i.e. in neuronally meaningful time scales. To solve this issue, multi-locus TMS (mTMS) technology has enabled electronic adjustments of the cortical target without physically moving the coil arrays (Nieminen *et al* 2022). mTMS provides fast and accurate adjustment of the stimulation parameters inside the scanner and between imaging sequences for human (Navarro de Lara *et al* 2023) and preclinical (Souza *et al* 2023) applications. However, the simultaneous use of many coils may result in an even higher stress than in a single coil due to Lorentz force summation. Specifically, in ultra-high-field 9.4 T MRI for small animals (Souza *et al* 2023), mTMS coils are exposed to extreme mechanical stress; a durable material and appropriate winding design is required to enable safe long-term use. To our knowledge, the mechanical behavior of mTMS coils in an MRI scanner has not been studied in detail before.

In this study, we aimed to assess the mechanical stress dynamics on human and small-animal mTMS coil arrays inside MRI scanners. We sought to analyze the coils' mechanical behavior on a microsecond time scale during and after stimulation pulses in high static magnetic fields (3 and 9.4 T). Our study proposes new insights for more durable and safer TMS coil designs suitable for combined brain stimulation and neuroimaging.

2. Materials and methods

For analyzing the mechanical behavior of mTMS coils inside an MRI scanner, the equations of Lorentz force and von Mises stress are presented below, followed by a detailed description for building the computational models.

2.1. Lorentz force, von Mises stress, and deformation

During the stimulation, a current through one TMS coil generates a magnetic field, $\mathbf{B}_{\text{coil}}$. The Lorentz force density on the coil can then be calculated by:

$$\mathbf{F}_{\text{lorentz}} = \mathbf{J} \times (\mathbf{B}_{\text{coil}} + \mathbf{B}_0)\,, \tag{1}$$

where $\mathbf{J}$ is current density in the coil wire and $\mathbf{B}_0$ is the is the external magnetic flux density (Crowther *et al* 2012). When two overlapping coils are used simultaneously, the Lorentz forces acting on the top and bottom coils, $\mathbf{F}'_{\text{top}}$ and $\mathbf{F}'_{\text{bottom}}$, respectively, are derived from equation (1) as:

$$\mathbf{F}'_{\text{top}} = \mathbf{J}_{\text{top}} \times \left(\mathbf{B}_{\text{top}} + \mathbf{B}_{\text{bottom}} + \mathbf{B}_0\right) \tag{2}$$

$$\mathbf{F}'_{\text{bottom}} = \mathbf{J}_{\text{bottom}} \times \left(\mathbf{B}_{\text{top}} + \mathbf{B}_{\text{bottom}} + \mathbf{B}_0\right). \tag{3}$$

Von Mises stress is a measure used to predict material yielding under various loading conditions by combining normal and shear stresses into an equivalent stress value (Callister and Rethwisch 2018). To obtain the von Mises stress distribution in the coil plate, the components of the Maxwell stress tensor σ_{ij} (Crowther *et al* 2013), which depict the relationship between electromagnetic forces and mechanical momentum, must be computed by:

$$\sigma_{ij} = \varepsilon_0 \left(E_i E_j - \frac{1}{2}\delta_{ij}E^2\right) + \frac{1}{\mu_0}\left(B_i B_j - \frac{1}{2}\delta_{ij}B^2\right), \tag{4}$$

where ε_0 is the permittivity of free space, μ_0 is the vacuum permeability, δ_{ij} is the Kronecker delta (which is 1 if $i = j$ and zero otherwise), E_i is the induced electric field, and B_i is the magnetic field along coordinate axis i.

In three dimensions, the stress in the material is represented by the stress tensor σ:

$$\sigma = \begin{bmatrix} \sigma_{xx} & \sigma_{xy} & \sigma_{xz} \\ \sigma_{yx} & \sigma_{yy} & \sigma_{yz} \\ \sigma_{zx} & \sigma_{zy} & \sigma_{zz} \end{bmatrix}. \tag{5}$$

The dynamic equilibrium equation gives the displacement vector $\mathbf{u}$ (COMSOL Multiphysics 2018) for computing the deformation of the coil plates at time t:

$$\nabla \cdot \sigma + \mathbf{F}_{\text{Lorentz}} = \rho \frac{\partial^2 \mathbf{u}}{\partial t^2}, \tag{6}$$

where ρ is the material density.

The stress tensor σ is related to the strain tensor $\mathbf{N}$ through the linear constitutive relation:

$$\sigma = \mathbf{C} : \mathbf{N}, \tag{7}$$

where $\mathbf{C}$ is the fourth-order elasticity tensor, representing the stiffness of the material, and the double dot product is $\mathbf{C} : \mathbf{N} = C_{ij}N_{ij}$. The strain tensor $\mathbf{N}$ is related to the displacement field $\mathbf{u}$ by:

$$\mathbf{N} = \frac{1}{2}\left(\nabla \mathbf{u} + (\nabla \mathbf{u})^T\right). \tag{8}$$

Using the finite element method, the domain and time are discretized, leading to solving a system of equations:

$$\mathbf{M}\ddot{\mathbf{U}} + \mathbf{D}\dot{\mathbf{U}} + \mathbf{K}\mathbf{U} = \mathbf{F}_{\mathbf{Lorentz}}(t), \tag{9}$$

where the mass matrix $\mathbf{M}$ represents the distribution of mass throughout the structure, the damping matrix $\mathbf{D}$ accounts for energy dissipation in the system, the stiffness matrix $\mathbf{K}$ represents the material and structural stiffness, and the force vector $\mathbf{F}_{\mathbf{Lorentz}}(t)$ represents the time-dependent Lorentz force acting on the structure. Finally, this system is solved iteratively to find the nodal displacements $\mathbf{U}(t)$ over time. For an in-depth explanation, see (COMSOL Multiphysics® 2021).

Based on the stress tensors, the scalar value for von Mises stress (Crowther *et al* 2013) is obtained as in:

$$s = \sqrt{\sigma_{xx}^2 + \sigma_{yy}^2 + \sigma_{zz}^2 - \sigma_x\sigma_y - \sigma_x\sigma_z - \sigma_y\sigma_z + 3\left(\sigma_{xy}^2 + \sigma_{yz}^2 + \sigma_{zx}^2\right)}. \tag{10}$$

2.2. Geometries for computational modeling

The 3D coil arrays were modeled and simulated in COMSOL Multiphysics® 6.0 (COMSOL, Inc., Burlington, MA, USA).

2.2.1. Rat mTMS coil array

The method for designing the winding paths for the rat mTMS coil array is described in (Souza *et al* 2023). Each coil was designed with two winding layers, with 1.6 mm between the wire centers. The wire paths were 3D-modeled with a circular profile (1.3 mm diameter). The top and bottom coils were wound in rectangular plates (length: 18.5 cm, width: 9.6 cm) of 7- and 10 mm thicknesses and separated by a 2 mm gap. The mTMS coil arrays were placed inside a cylindrical air domain (30 cm diameter, 50 cm length) with a 9.4 T homogeneous static magnetic field to simulate the MRI bore, such that the direction of the MRI field was parallel to the plates representing the experimental setup using 9.4 T 31 cm-bore MRI system reported in (Souza *et al* 2023). To enable current flow in a closed path, the coil wires were extended from the plates to the walls of the air domain, as shown in figure 1. We set the coils as 'homogeneous multiturn' with 40 turns (diameter of each wire strand: 0.2 mm) to closely represent the litz wire consisting of 40 individual strands in our coils; thus, the current in each wire strand was divided by 40.

To accurately represent real-life applications, we excluded the wires outside the coil plates from the mechanical simulations. The mTMS coil plates were fixed by applying a spring boundary condition to one side of the plates (highlighted in blue in figure 1(a)), with a spring constant per unit area of 1 N $(\text{mm})^{-2}$. This condition mimics attachment to a support structure that behaves like a loose spring, allowing free plate movements. The fixation approach was based on the guidelines from COMSOL Multiphysics® (see Frei 2021) and to match the fixation of the protective casing used in our experimental setup. In this

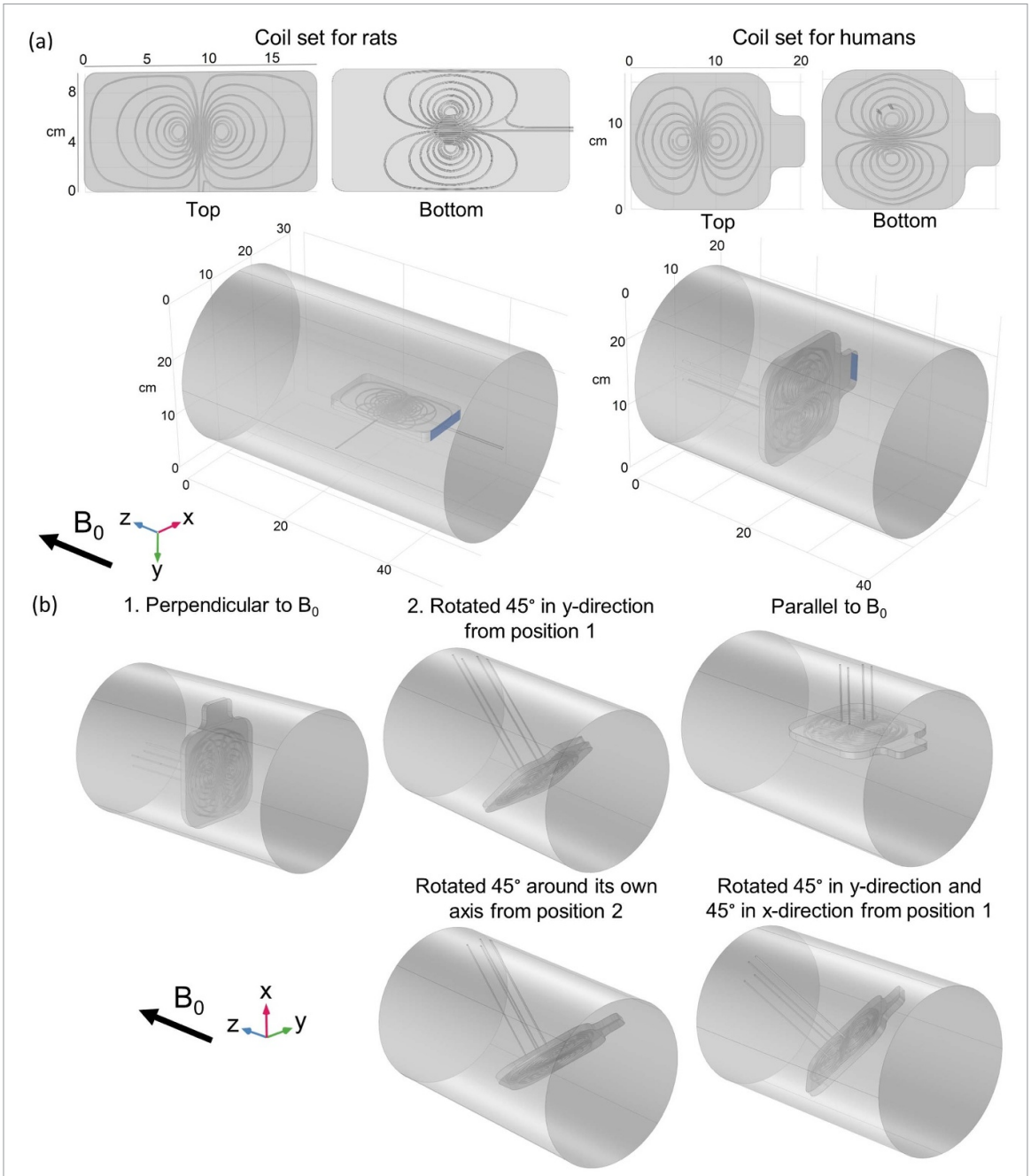

Figure 1. (a) Rat and human mTMS coil array models in our simulations. The fixed edges are highlighted in blue. (b) The placements of the human mTMS coil array relative to the external magnetic field.

configuration, the coil set was placed flat inside a protective casing (see section 2.6), enabling nearly unconstrained movement, although the casing was anchored at the back handle. Frei (2021) introduces techniques for simplifying the modeling process by approximating the effects of surrounding fixtures through boundary loads. This is achieved by applying equal and opposite forces to the component's boundaries, allowing for accurate stress and deformation analysis without considering the component's overall movement. The spring constant was carefully chosen to be large enough for system stability yet small enough to avoid impacting the solution. This decision was confirmed by testing two other methods described in Frei (2021), which yielded nearly identical stress and displacement results.

2.2.2. Human mTMS coil array

The winding paths for the human mTMS coil array were obtained from (Souza *et al* 2022)., consisting of two overlapping figure-of-eight coils with 12 windings each and with a 90° relative angle. Each coil for the human coil array was made in two layers 2.6 mm apart, and the wires were modeled with a rectangular profile (2.6 mm width, 2.4 mm height). The top and bottom coils were placed each in a solid casing (160 mm width, 160 mm height, 9 mm thickness) 0.5 mm apart. The human coil array was placed in a cylindrical air

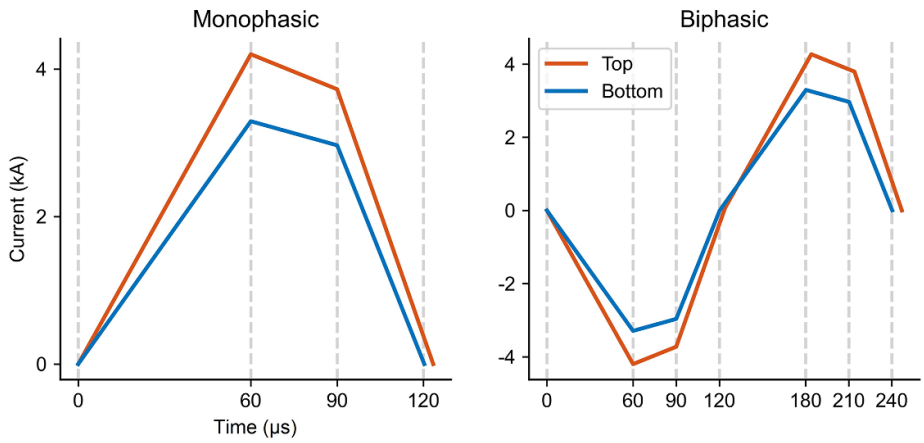

Figure 2. Monophasic and biphasic current waveforms to simulate the mTMS pulses.

domain (26 cm diameter, 40 cm length) with a 3 T homogeneous static magnetic field, such that the ends of the coil wire were connected to the walls of the air domain. To investigate the effect of different angles between the coil plane and the direction of the static magnetic field, we performed simulations with five coil array placements (shown in figure 1(b)). Both coils were set as 'homogeneous multiturn' with 70 turns to represent the litz wire consisting of 70 individual strands in the human coil design, and the current in each wire strand was divided by 70. The wires outside the coil plates were again excluded from the structural mechanics calculations, and the wires outside the plates were excluded from the mechanical calculations. The coil plates were fixed by applying a spring boundary condition to the handle (highlighted in blue in figure 1(a)) with a spring constant per unit area of 1 N m^{-3}.

Two triangular mesh elements were added to the end faces of each coil and swept through the coil winding paths, resulting in triangular prisms with a maximum length of 1 mm. The outer coil surfaces were discretized in triangular elements to automatically build tetrahedral meshes and model the plates and air domains.

2.3. Current waveforms

TMS pulse waveforms were modeled as mono- and biphasic to compare their effect on the mechanical behavior of the coil arrays. The waveforms were approximated as piecewise linear functions (figure 2), such that the magnitude of the induced E-field would be similar in each phase, considering the increased distance of the top coils relative to the cortical surface. The monophasic waveform had rise, hold, and fall times set to 60, 90, and 120 μs, respectively (Souza *et al* 2023). In turn, the biphasic waveform consisted of six parts with durations of 60, 90, 120, 180, 210, and 240 μs. The current parameters of the biphasic pulse were adjusted to induce the same electric field intensity in each rise, hold and fall phase as in the monophasic pulse. The coil current was zero from the end of the pulse until the end of the simulation period ($t = 1000$ μs); the simulations were performed at time steps of 5 μs.

2.4. Coil plate materials

We simulated the mechanical behavior of six different thermoplastic coil plates having suitable material properties for TMS–MRI applications. The assessed plastics were polycarbonate (PC), polyether ether ketone (PEEK), acrylonitrile butadiene styrene (ABS), two types of glass-filled (GF) polyamide (PA), and polyoxymethylene (POM). The material properties were obtained from Granta EduPack 2022 R1 database (ANSYS, Inc., Canonsburg, PA, USA), except for PA 40% GF, of which the density, Young's modulus and tensile stress were obtained from Protolabs (Proto Labs, Inc., Maple Plain, MN, USA, material name: PA12 40% GF (PA614-GS)). The remaining properties were estimated based on similar materials from Granta EduPack. All material properties (shown in table 1) were computed as the range average, assuming a linear behavior on the microsecond-level timescale of the simulations. Because the plate's electrical conductivity does not influence the mechanical simulations, it was set to 0.01 Ω m^{-1} for all materials. We used 30% glass-fiber-filled (PA 30% GF) PA for the human coil plate due to the superior durability in the rat coil simulations compared to the other materials.

Table 1. Mechanical and electronic properties of the coil plates in the simulations.

Material	PC	PEEK	ABS	PA 30% GF	PA 40% GF	POM
Density (g cm^{-3})	1.18	1.31	1.05	1.36	1.22	1.4
Relative permittivity	3.2	3.2	3	12.15	12	3.7
Electrical conductivity (Ω m^{-1})	5.50×10^{-13}	1.67×10^{-14}	1.82×10^{-20}	2.08×10^{-12}	1.0×10^{-15}	1.83×10^{-19}
Young's modulus (MPa)	2220	3855	2450	7550	3600	2900
Poisson's ratio	0.39	0.4	0.38	0.36	0.35	0.39
Tensile strength (MPa)	66.2	107.0	40.0	125.5	48.0	80.5
Flexural strength (MPa)	89.6	110.5	60.0	195.5	65.0	89.8

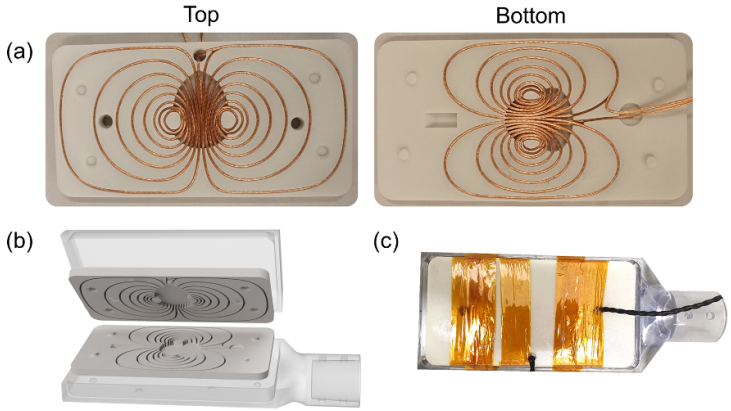

Figure 3. (a) Coil plates wound with litz wire before being potted with silicone. (b) 3D model of the coil plates and the protective holder case. Adapted from Souza *et al* (2023). CC BY 4.0. (c) Photo of the coil array taped on the holder.

2.5. Outlier removal

We observed unrealistically high stress values in individual data points from the simulation, possibly due to the coarse mesh compared to the model complexity (Naganarayana and Prathap 1992). COMSOL provides a smoothing feature when displaying results in 2D and 3D, which are not applied to the exported data. These singularities were removed from the exported stress data using a z-score outlier removal method (Rousseeuw and Hubert 2018). We used $z = 5$ as a threshold value because it provided the closest correspondence with COMSOL smoothed visualization. Only 0.002% of the stress data points were removed as outliers; the results are reported with data after outlier removal.

2.6. mTMS–fMRI experimental verification of the rat coil arrays

To test the durability of different materials, we built two different coil arrays for rats. Because the material with the highest durability based on the simulations (PA 30% GF) was unavailable from our suppliers, we chose the second-best option, PEEK. For a material with lower durability, we used PA 40% GF.

The coil plates were CNC-machined (PEEK) or 3D-printed with selective laser sintering (PA 40% GF). We wound the coils with copper litz wire (1.7 mm diameter; 3-layer Mylar coating; Rudolf Pack GmbH & Co. KG, Gummersbach, Germany) in the plates' grooves. The wires were pushed tightly in the grooves and against each other; thus, we had to use a smaller wire diameter in the simulations to avoid the wires from overlapping. Each pair of coil plates was potted with a 2-component silicone-based elastomer (SYLGARD® 184, Dow Inc., Midland, MI, USA). The wire ends were crimped with M6-sized adapters for connecting them to the mTMS power electronics cabinet through a connector box (Souza *et al* 2023). For additional safety, we wrapped the coil array in a custom-made PC case with Kapton tape (figure 3).

Each coil array, one at a time, was connected to our 2-channel mTMS power electronics and placed inside a 9.4 T MRI magnet (bore diameter 31 cm; Agilent Technologies, Inc., USA). First, a single current pulse with an intensity of 250 A was given, after which we observed the physical condition of the coil plates. If no signs of breakage were visible, the intensity of the current pulse was increased, and the stimulation was repeated with intensities of 500, 1000, and 1500 A. The monophasic pulses (time steps: 60, 90, and 120 μs, see figure 2) were first given to top and both coils, after which we proceeded to biphasic pulses (time steps: 60, 90, 120, 180, 210, and 240 μs, see figure 2). The pulse waveforms illustrated in figure 2 are the ideal representation whereas the real waveforms might have had some distortions due to the inductance of the wires. We did not run pulses through the bottom coil separately because our preliminary simulations had shown that the coil plates would withstand the forces produced by the bottom coil alone.

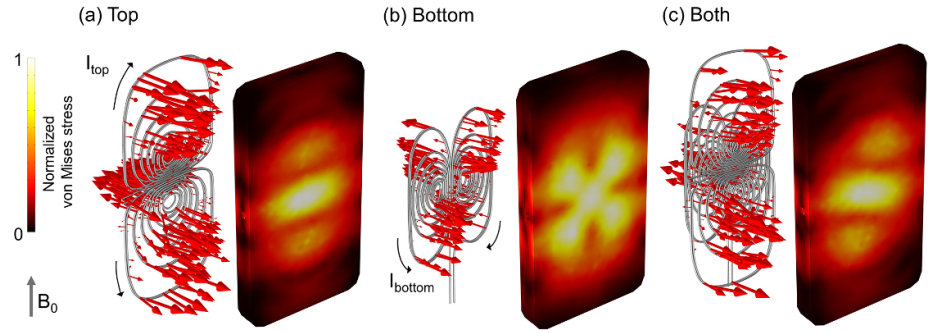

Figure 4. The Lorentz force (red arrows) in the PEEK coil array at 60 μs during a biphasic current pulse applied to the (a) top coil, (b) bottom coil, and (c) both coils together. The corresponding normalized von Mises stresses on the coil plates are depicted with heatmaps. The black arrows (I_{top}, I_{bottom}) indicate the current flow direction in the coils; B_0 is the direction of the static magnetic field in the MRI bore.

3. Results

3.1. Stress distribution and plate displacement

Figure 4 illustrates the Lorentz force vectors in the rat coils due to the interaction between the TMS pulse and the static MRI field ($\mathbf{B}_0$). When the TMS pulse is applied to the top coil alone, the strongest forces (longest vectors) are concentrated on the central part of the figure-of-eight coil, where the current runs perpendicular to the static magnetic field (figure 4(a)). Lorentz forces pull the wires to the opposite direction on the outer loops, creating horizontal areas with higher stress on the coil plate. The stress distribution resulting from firing the bottom coil has an X shape, where the diagonal components have forces in opposite directions (figure 4(b)). When both coils are activated simultaneously, the stress pattern on the plates is mostly concentrated in the middle while also having slightly rotated diagonal components as the sum of forces from both coils (figure 4(c)).

In figure 5, the stress distributions in a PEEK coil array are visualized at various time instants during and after the current pulses. A TMS pulse applied to the bottom coil alone results in up to 60% lower stress than when the top or both coils are used. After each pulse is given, the plates start vibrating as seen from the time-dependent propagation of the stress patterns.

Despite the similar current amplitudes in the mono- and biphasic pulses, the shape of the waveform affects the magnitudes of the maximum stresses on the coil plates. Figure 5 shows that the maximum stress reaches up to 100 MPa after the biphasic pulse ($t = 240$ μs; $t = 650$ μs), whereas the monophasic pulse results in a maximum stress of approximately 80 MPa at $t = 340$ μs.

3.2. Maximum stress over time

Figure 6 shows the maximum stress and plate displacement values over time for all the materials, coil combinations, and current waveforms when the top and bottom plates are considered as a single object. As the Lorentz force is in a direction normal to the coil plane, it causes the plates to flex in different directions. Thus, we considered the instant when the von Mises stress exceeds the material's flexural strength to indicate that the coil plates would break (Callister and Rethwisch 2018).

The stress and maximum displacement vary with different timings and peak values for each material, as illustrated in figure 6, indicating a shock wave resulting from the current pulses propagating at distinct speeds in the coil plates. The stress and displacement are up to 120% higher when the top coil alone or both coils are activated compared to the bottom coil alone. When the top or both coils are activated, the maximum stress on the plate exceeds the flexural strength for all materials, except for PA 30% GF and PEEK. In turn, with the bottom coil alone, the flexural strength is not exceeded on any of the materials.

With the monophasic pulse, the peak stress continuously increases until the end of the hold phase at about 90 μs, after which it slightly decreases. Each trapezoidal phase in the current waveform produces a peak in the von Mises stress. However, the maximum stress occurs after the pulses are given, between 245 and 380 μs for the monophasic and between 550 and 1000 μs for the biphasic pulse. The biphasic pulse induces higher stress values than the monophasic pulse, and the differences in the stress amplitudes vary between the coil-plate materials. For instance, the difference in the maximum stresses between the mono- and biphasic pulses is 4.5% for PA 30% GF, whereas for PC, the difference reaches 34%.

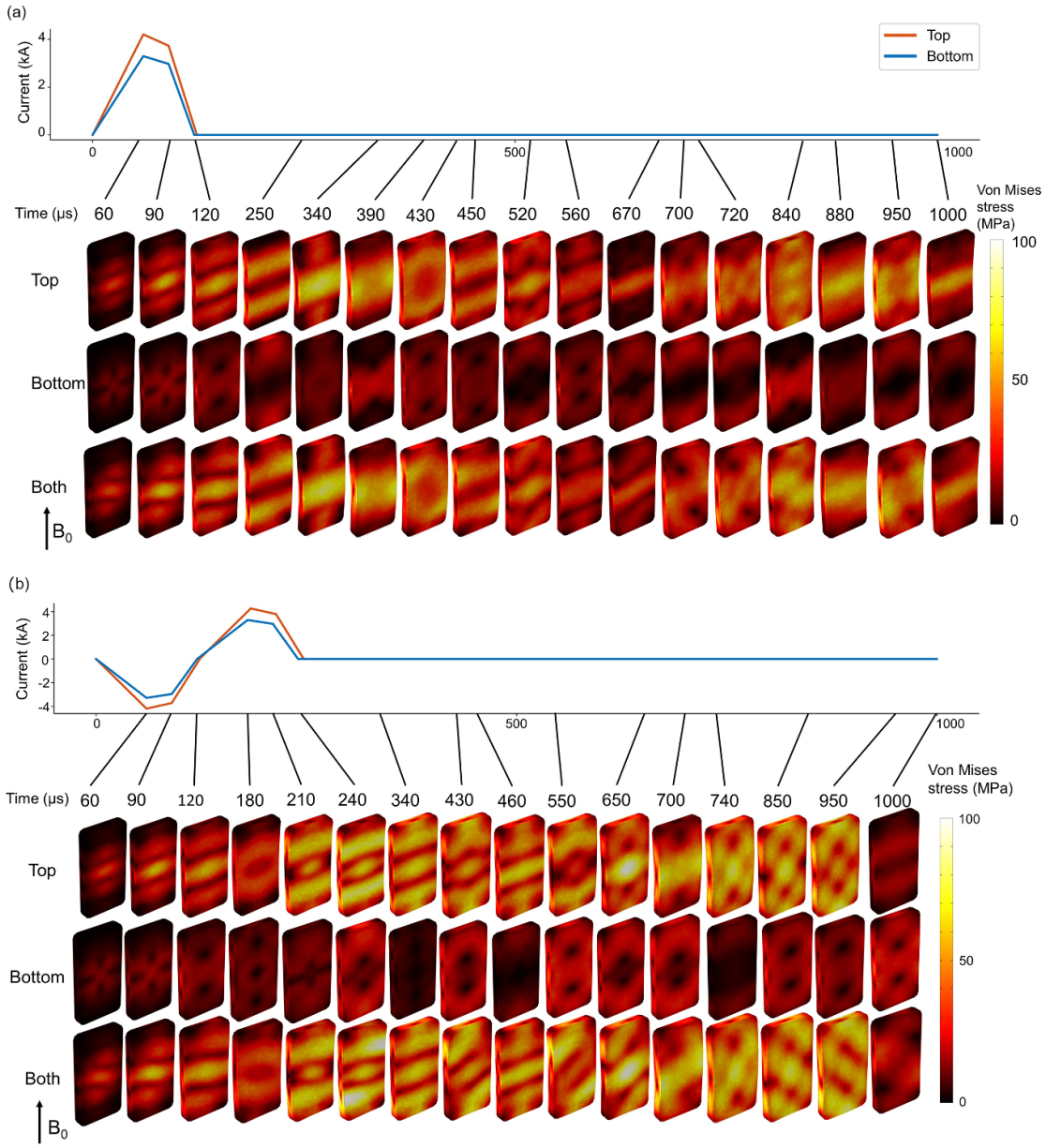

Figure 5. The stress distribution and corresponding deformation of the PEEK plates when (a) monophasic and (b) biphasic current pulse is driven through the top and bottom coils separately, and through both coils together. The surface of the top coil plate is displayed at the front, B_0 is the direction of the static magnetic field in the MRI bore. The von Mises stress on the coil plates is shown using the same color range for all plots; the deformations can be seen from the plate displacements.

Table 2 displays the maximum stress from each simulation. According to our calculations, the most durable materials were PA 30% GF and PEEK, for which the maximum stress did not exceed the flexural strength.

3.3. Spatial distribution of maximum stress

Figure 7 displays the locations of the maximum stress in each simulation. With the monophasic pulse, the maximum stress is near the center of the coil surface for the least durable materials (ABS, POM, PC). In turn, for the most durable materials (PA 30% GF, PEEK) and PA 40% GF, the maximum stress is on the outermost windings of the top coil. Notably, the current waveform and coil combination affected the maximum stress location. With the monophasic pulse on the bottom coil alone, the highest stress is at the surface of the bottom wire grooves. For the other coil combinations with a monophasic pulse, the highest stress is located close to the top wires and the surface of the top plate. With the biphasic pulse, the highest stress is towards the outermost coil windings, regardless of the coil combination.

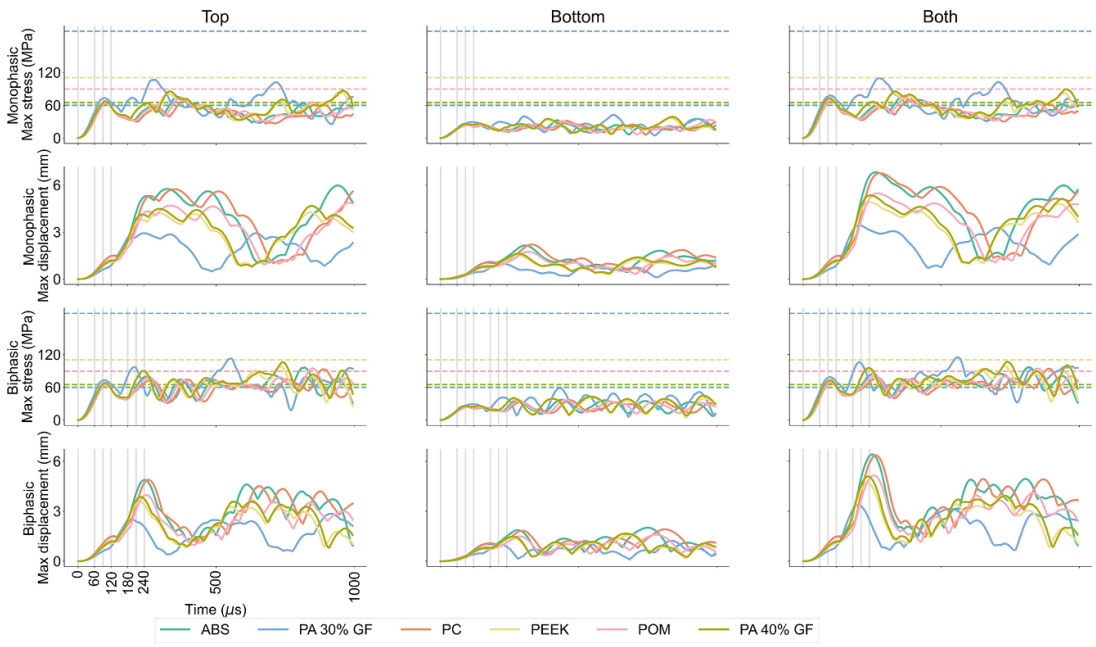

Figure 6. Maximum stresses and displacements on the plates over time for each pulse and coil combination. The vertical lines mark the timings of the current pulse phases; the flexural strength of each material is shown with the horizontal dashed lines. Different materials are shown with different colors.

Table 2. Maximum stress in the coil plates. The ratios in percentage between the simulated maximum stress and the flexural strength are given in parentheses. The color-shaded cells highlight stress values exceeding the materials' flexural strength.

Material/Flexural strength (MPa)	Monophasic			Biphasic		
	Top	Bottom	Both	Top	Bottom	Both
PA 30% GF/195.5	107 (55)	43 (21)	109 (56)	113 (58)	59 (30)	115 (59)
PC/89.6	71 (79)	32 (35)	71 (80)	93 (104)	37 (41)	94 (105)
PEEK/110.5	85 (77)	36 (33)	82 (75)	93 (84)	42 (38)	99 (90)
POM/89.8	74 (83)	33 (37)	74 (82)	95 (106)	37 (41)	94 (105)
ABS/60.0	76 (126)	35 (58)	76 (126)	97 (161)	37 (62)	97 (161)
PA 40% GF/65.0	87 (134)	39 (60)	89 (138)	106 (163)	45 (69)	107 (165)

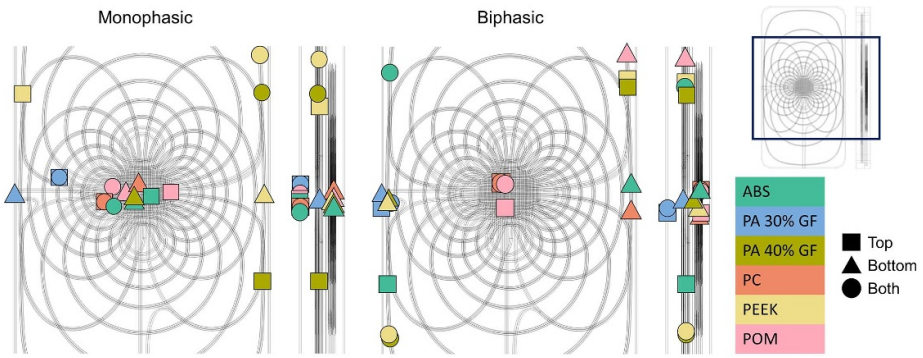

Figure 7. Maximum stress locations shown from top and side views of the coil plane. The coil current combinations are shown with different symbols and the plate materials are indicated by different colors corresponding to figure 6.

3.4. Experimental characterization of the rat mTMS coil arrays at 9.4 T

All mTMS coil arrays in the test setup at 9.4 T were fractured with smaller current amplitudes than those predicted in the simulations. The PA-40%-GF top and bottom plates fractured with the biphasic pulse at 1500 A (36% of maximum stimulator output, MSO, of 4200 A) on both coils. Small fractures were formed in the middle part of the top plate surface, and a major crack around the center of the bottom plate (figures 8(a)

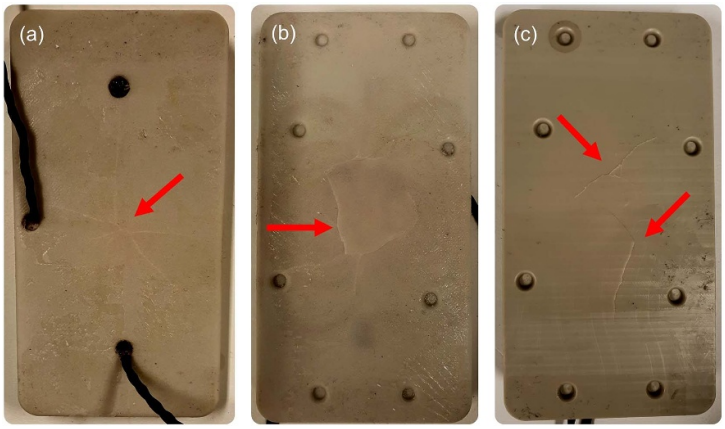

Figure 8. Fractures (indicated with red arrows) in the mTMS coil plates for rats. Top surface of (a) PA 40% GF, bottom surface of (b) PA 40% GF and (c) PEEK.

and (b)). The PEEK coil plates broke during a monophasic current pulsed through both coils at 1000 A (24% MSO), resulting in two long cracks near the middle of the bottom coil surface (figure 8(c)).

3.5. mTMS coil array for humans

Our simulations indicate that the mTMS coil array for humans with PA-30%-GF plates (flexural strength: 196 MPa) could withstand the biphasic current pulses ran through both coils, regardless of the coil position relative to the 3 T static magnetic field. The smallest stress amplitude, 12 MPa, was obtained with the coil planes perpendicular to $\mathbf{B}_0$ (figure 9(a)). In turn, the highest stress amplitudes occur when the coil planes are rotated 45° in two perpendicular axes (69 MPa; figure 9(e)) or parallel relative to $\mathbf{B}_0$ (62 MPa; figure 9(c)), with a drastic increase of up to 457% from the lowest stress amplitude. When the coil planes are angled 45° relative to $\mathbf{B}_0$, the maximum stress on the coil plates reaches 45 MPa (figure 9(b)). If we rotate the coil array by 45° around its own axis from this position, the maximum stress decreases to 29 MPa (figure 9(d)).

According to figure 9(a), when the coil plane is perpendicular to the $\mathbf{B}_0$ field, the resulting Lorentz forces act radially inward or outward depending on the current flow direction in the coil. This leads to tension and compression parallel to the coil plane, causing lower stress on the plates compared to the other coil placements. On the contrary, the highest stresses are present when the Lorentz force vectors are normal to the coil plane (figures 9(b), (c) and (e)), producing a diagonal bending stress on the plates. In addition to the angle between the coil plane and $\mathbf{B}_0$ field. Also, the coil array orientation strongly influences the maximum stress amplitude due to the interplay between magnetic fields $\mathbf{B}_0$ and $\mathbf{B}_{\text{coil}}$, as shown in figures 9(b) and (d).

4. Discussion

We calculated the mechanical stress on realistic models of rat and human mTMS coil arrays inside an MRI bore. We performed time-dependent analyses, which enabled comparing the effects of different current waveforms on the spatiotemporal stress distributions. We demonstrated that different phases of the current waveforms produce shock waves that propagate in the coil plates and interfere with each other, resulting in various repeating stress patterns that depend on the material and current waveform. In addition, we compared the durability of potential materials for the coil plates and studied the effect of coil array placement relative to the external MRI field direction. Below, we provide suggestions for more durable MRI-compatible TMS coil array designs.

The results for the rat mTMS coil array showed that the bottom coil, which is closer to the cortical surface, produces lower stress amplitudes due to the almost 1 kA smaller current amplitude compared to the coil on top. The strongest Lorentz forces are located on the parts of the coils where the current runs perpendicular to the static magnetic field (figure 4) causing flexural stress on the coil plates, similar to (Crowther *et al* 2013). Because the coil that is further from the head needs a higher current for inducing a similar electric field in the cortex, the positions of the two coils could be exchanged such that the current pulses with a weaker amplitude would be fired through the coil with a more stress-evoking geometry.

Compared to previous studies with uniform (Crowther *et al* 2013) and continuous sinusoidal currents (Crowther *et al* 2012, Cobos Sánchez *et al* 2020, Afuwape *et al* 2021), we investigated the effect of two trapezoidal current waveforms during and after a single current pulse. We found that each linear phase in the current waveform (rise, hold, and fall) produces a shock wave that propagates back and forth in the coil plate

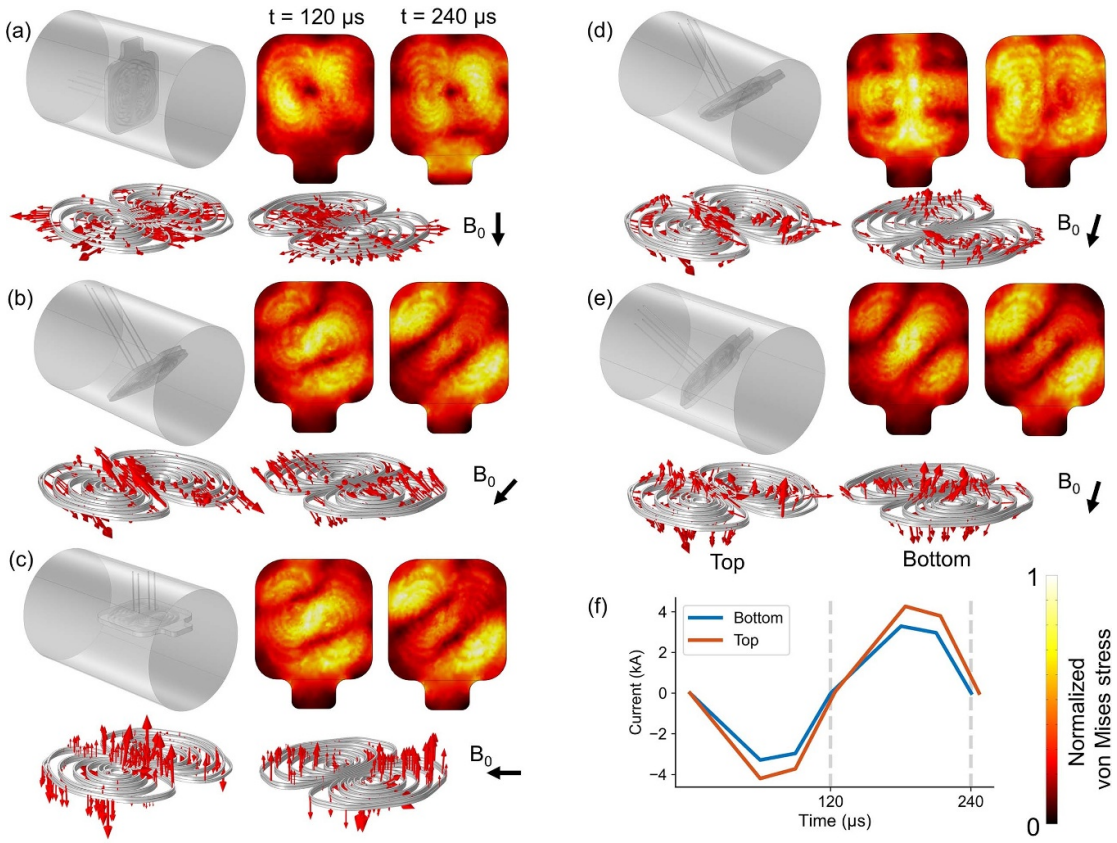

Figure 9. Normalized stress distributions on the coil plate's bottom surface at t = 120 μs and t = 240 μs. The red arrows show the normalized Lorentz force contribution on the top and bottom coils during the biphasic pulse (t = 120 μs). Panels (a)–(e) correspond to the coil orientations described in figure 1. (f) Biphasic current waveform as reproduced in figure 2.

and eventually interferes with the others. In both cases, the maximum stress occurs after the current has returned to 0 (shown in figure 6), which has not been reported in previous studies due to the lack of time-dependent models.

With monophasic current pulses, the locations of the maximum stresses in the rat coil plates were shown to depend on the plate material. However, with the biphasic current pulse, the maximum stress locations were instead sporadically located on the plate. Because the biphasic waveform has more current phase changes than the monophasic one, the resulting shock waves seem to result in more interference, which might explain these distributed maximum stress locations. Different material properties could also explain the differences in the maximum stress locations, leading to various shock wave propagation speeds. The dynamics of shock wave propagation and interference can be useful in finding optimal timings for the current waveform phases that would lead to destructive interference, lowering the stress amplitudes in the coil plates.

Our simulations with the human coil array showed that the Lorentz forces on the coils and the stress on the coil plates depend highly on the relative positioning of the coil plates with respect to the static MRI field. When the coil array is perpendicular to the MRI field, the Lorentz force vectors point radially inward and outward during the pulse, creating less stress because there is no bending force. Thus, to reduce bending forces in an experimental setting, the TMS coils should be aligned as perpendicularly as possible to the external magnetic field. Our results regarding the Lorentz force vectors are in line with previous studies (Crowther *et al* 2012, 2013, Cobos Sánchez *et al* 2020), in addition, we have produced a time-dependent assessment of the stress on the coil plates. In preclinical mTMS–MRI as the one reported by Souza *et al* (2023), it might be however challenging to adjust the coil array orientation relative to the static field due to the restricted bore space. Consequently, we did not test different coil placements for the rat coil set. However, the rat and human coil windings have similar effects from the forces because their windings have two overlapping figure-of-eight coils at a 90° relative angle. TMS coil arrays should be durable and extensively tested for safe applications in living animals; thus, further investigation of the stress in the rat coil set at different angles would be beneficial, particularly if there is a possibility for its use in a larger MRI bore.

Regarding our experimental tests, all the plates fractured in the middle part, which was shown to be a region with recurring high stresses in figure 5. The more durable plate material, PEEK, which was expected

to withstand the current pulses according to the simulations, fractured at a lower current amplitude than the less durable material, PA 40% GF, which indicates that our simulations might have underestimated the stress. This deviation might be due to the von Mises stress alone not being sufficient to predict a flexural fracture and due to the model approximations. For instance, the silicone glue layer between the plates and wires was ignored, and the coil plate materials were approximated as linear. The coarse mesh in our models resulted in high-stress singularities, causing inaccuracies in the stress data despite outlier removal. Opting for mesh refinement within the simulations and adding the silicone layer with its elastic properties to the 3D model would yield quantitative results that better approximate the experimental observations. In addition, the linear material properties could be replaced with measured nonlinear data, such as stress–strain curves. Our coils broke at lower current densities than the simulations predicted possibly partially because we used wires in the simulations that were 20% smaller in diameter compared to the ones in our real coils. Moreover, the simulations did not consider the potential damage caused by the cumulative effect of consecutive pulses. The quantitative results of our simulations, such as the maximum stress values and durability of each material, should thus be carefully interpreted. To enhance model precision and to achieve better correlation with experimental data, the wire diameter should match that of the actual coils, and the cumulative impact of consecutive pulses to the coil plate durability should be included in the simulations.

The best candidate out of the six materials modeled was found to be PA 30% GF, which would be an interesting candidate as the glass-fiber filling increases the durability for bending and the stiffness of the material. The applied load on the composite is transferred from the polymer matrix to the glass fibers, and the distribution of stress prevents the object from experiencing high levels of strain which would lead to local weaknesses and fracture (Callister and Rethwisch 2018).

5. Conclusion

We analyzed the time-dependent stress distribution in mTMS coil arrays operating inside an MRI scanner with high static magnetic fields for rat and human applications. We found that in addition to choosing a durable material to enclose the coil wires, the current waveforms, the coil alignment relative to the MRI static field, and the coil array design are important factors in achieving a safer and more durable instrumentation for concurrent TMS–MRI applications. Mechanical and electromagnetic simulations provide valuable insight into the performance of novel TMS coil designs in different conditions, enabling safer research and clinical applications.

Data availability statement

The data that support the findings of this study are available upon reasonable request from the authors.

Acknowledgments

This project has received funding from the Jane and Aatos Erkko Foundation, Emil Aaltonen Foundation, the Academy of Finland (Decisions No. 294625 and 349985), and the European Research Council (ERC Synergy) under the European Union's Horizon 2020 research and innovation programme (ConnectToBrain; Grant Agreement No 810377). We acknowledge the computational resources provided by the Aalto Science-IT project.

Conflict of interest

RJI has patents and patent applications on mTMS technology. HS and VHS are inventors of patent applications for TMS technologies. The other authors have no competing interests.

ORCID iDs

Maria A Koponen https://orcid.org/0009-0009-5335-9344
Juuso T Korhonen https://orcid.org/0000-0001-7802-7084
José A Vilchez Membrilla https://orcid.org/0000-0002-3383-2634
Heikki Sinisalo https://orcid.org/0009-0000-0037-8378
Jaakko Paasonen https://orcid.org/0000-0002-1529-596X
Clemente Cobos Sánchez https://orcid.org/0000-0003-0299-5358
Olli Gröhn https://orcid.org/0000-0003-1372-1651
Risto J Ilmoniemi https://orcid.org/0000-0002-3340-2618
Victor H Souza https://orcid.org/0000-0002-0254-4322

References

Afuwape O F, Kiarie W M, Bentil S A and Jiles D C 2021 Mechanical analysis of the quadruple butterfly coil during transcranial magnetic stimulation and magnetic resonance imaging *43rd Annual Int. Conf. IEEE Engineering in Medicine & Biology Society (EMBC)* (https://doi.org/10.1109/EMBC46164.2021.9629750)

Bergmann T O, Varatheeswaran R, Hanlon C A, Madsen K H, Thielscher A and Siebner H R 2021 Concurrent TMS-fMRI for causal network perturbation and proof of target engagement *NeuroImage* **237** 118093

Callister W D and Rethwisch D G 2018 *Materials Science and Engineering: An Introduction* 10th edn (Wiley)

Chail A, Saini R K, Bhat P S, Srivastava K and Chauhan V 2018 Transcranial magnetic stimulation: a review of its evolution and current applications *Ind. Psychiatry J.* **27** 172–80

Cobos Sánchez C, Ruiz Cabello M, Quiros Olozábal Á and Fernández Pantoja M 2020 Design of TMS coils with reduced Lorentz forces: application to concurrent TMS-fMRI *J. Neural Eng.* **17** 016056

COMSOL Multiphysics® 2021 Analysis of deformation 11 March (available at: www.comsol.com/multiphysics/analysis-of-deformation?parent=structural-mechanics-0182-192) (Accessed 13 June 2024)

COMSOL Multiphysics 2018 Introduction to structural mechanics (available at: www.comsol.com/multiphysics/introduction-to-structural-mechanics) (Accessed 18 September 2023)

Crowther L J, Porzig K, Hadimani R L, Brauer H and Jiles D C 2012 Calculation of Lorentz forces on coils for transcranial magnetic stimulation during magnetic resonance imaging *IEEE Trans. Magn.* **48** 4058–61

Crowther L J, Porzig K, Hadimani R L, Brauer H and Jiles D C 2013 Realistically modeled transcranial magnetic stimulation coils for Lorentz force and stress calculations during MRI *IEEE Trans. Magn.* **49** 3426–9

Frei W 2021 Modeling parts without constraints in your structural analyses 7 January (COMSOL Multiphysics®) (available at: www.comsol.com/blogs/modeling-parts-without-constraints-in-your-structural-analyses) (Accessed 11 June 2024)

Iglesias A H 2020 Transcranial magnetic stimulation as treatment in multiple neurologic conditions *Curr. Neurol. Neurosci. Rep.* **20** 1–9

Ilmoniemi R J, Ruohonen J and Karhu J 1999 Transcranial magnetic stimulation—a new tool for functional imaging of the brain *Crit. Rev. Biomed. Eng.* **27** 241–84

Koponen L M, Nieminen J O and Ilmoniemi R J 2015 Minimum-energy coils for transcranial magnetic stimulation: application to focal stimulation *Brain Stimul.* **8** 124–34

Koponen M 2023 Mechanical modeling of multi-coil transducers for brain stimulation in high static magnetic fields *MSc Thesis* University of Helsinki (available at: http://urn.fi/URN:NBN:fi:hulib-202303161484)

Lee H-J, Woudsma K J, Ishraq M F and Lin F-H 2023 Design of coil holder for the improved maneuvering in concurrent TMS-MRI *Brain Stimul.* **16** 966–8

Mizutani-Tiebel Y, Tik M, Chang K-Y, Padberg F, Soldini A, Wilkinson Z, Ci Voon C, Bulubas L, Windischberger C and Keeser D 2022 Concurrent TMS-fMRI: technical challenges, developments, and overview of previous studies *Front. Psychiatry* **13** 825205

Moisa M, Pohmann R, Ewald L and Thielscher A 2009 New coil positioning method for interleaved transcranial magnetic stimulation (TMS)/functional MRI (fMRI) and its validation in a motor cortex study *J. Magn. Reson. Imaging* **29** 189–97

Naganarayana B P and Prathap G 1992 Expert systems and finite element structural analysis—a review *Sadhana* **17** 275–98

Navarro de Lara L I, Stockmann J P, Meng Q, Keil B, Mareyam A, Uluç I, Daneshzand M, Makarov S, Wald L L and Nummenmaa A 2023 A novel whole-head RF coil design tailored for concurrent multichannel brain stimulation and imaging at 3T *Brain Stimul.* **16** 1021–31

Nieminen J O *et al* 2022 Multi-locus transcranial magnetic stimulation system for electronically targeted brain stimulation *Brain Stimul.* **15** 116–24

Rousseeuw P J and Hubert M 2018 Anomaly detection by robust statistics *Wiley Interdiscip. Rev.: Data Min. Knowl. Discov.* **8** e1236

Seewoo B J, Etherington S J, Feindel K W and Rodger J 2018 Combined rTMS/fMRI studies: an overlooked resource in animal models *Front. Neurosci.* **12** 180

Souza V H, Nieminen J O, Tugin S, Koponen L M, Baffa O and Ilmoniemi R J 2022 TMS with fast and accurate electronic control: measuring the orientation sensitivity of corticomotor pathways *Brain Stimul.* **15** 306–15

Souza V H, Sinisalo H, Korhonen J T, Paasonen J, Nyrhinen M, Nieminen J O, Koponen M, Kettunen M, Gröhn O and Ilmoniemi R J 2023 A multi-channel TMS system enabling accurate stimulus orientation control during concurrent ultra-high-field MRI for preclinical applications *bioRxiv Preprint* https://doi.org/10.1101/2023.08.10.552401 (Accessed 14 August 2023)